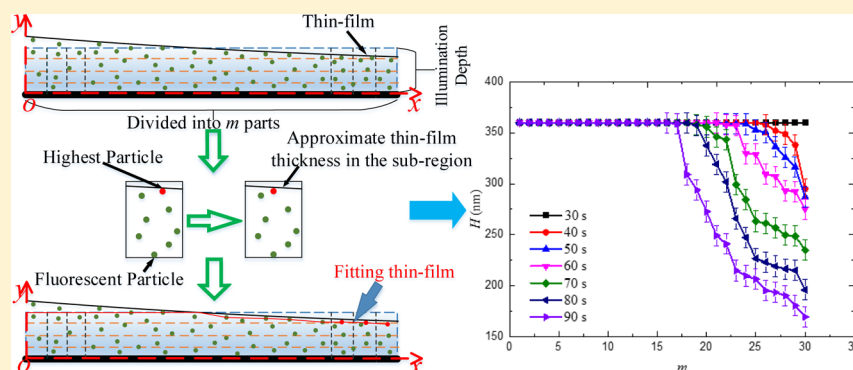


Fluid Flow and Thin-Film Evolution near the Triple Line during Droplet Evaporation of Self-Rewetting Fluids

 Yang Yang, Leping Zhou,*[✉] Xiaoze Du, and Yongping Yang

Key Laboratory of Condition Monitoring and Control for Power Plant Equipment of Ministry of Education, School of Energy, Power and Mechanical Engineering, North China Electric Power University, Beijing 102206, China



ABSTRACT: The microscopic region near the triple line plays an important role in the heat and mass transfer of droplets, although the mechanisms of evaporation and internal flow remain unclear. This paper describes an experimental study of fluid flow and thin-film evolution near the triple line in sessile droplets of self-rewetting fluids, aqueous solutions of alcohols with the number of carbon atoms varying from 1 to 7, to analyze the influence of various factors on the mesoscale flows. The mechanism of internal flow for self-rewetting fluid droplets was different from that of conventional fluids, and hence, a novel expression of the in-plane average velocity was fitted for them. The temporal and spatial evolution of the thin-film thickness near the triple line during droplet evaporation was obtained by using a proposed subregion method, which was developed from an evanescent-wave-based multilayer nanoparticle image velocimetry technique. The self-rewetting fluids are conducive to increase the microscopic critical contact angle and the energy barrier of the contact line, which reduces the rate of thin-film thickness variation. The inhibited impact of self-rewetting fluids on evaporation increases gradually with an increasing number of carbon atoms.

1. INTRODUCTION

Droplet evaporation widely exists in daily life and industrial applications such as dropwise cooling, spray cooling, and fuel injection. The evaporation of a sessile droplet suspended with nanoparticles plays a crucial role in engineering, including inkjet printing, coatings, and optoelectronic device manufacturing.^{1–3} The movement and deposition of nanoparticles in a droplet were believed to be controlled by the fluid flow, especially the contact line pinning or depinning motion on the solid surface.^{4,5} However, the internal flow of an evaporating droplet may be influenced by various factors, including the capillary flow induced by surface tension and the Marangoni flow that resulted from the temperature gradient or the solute concentration gradient along the liquid–vapor interface.⁶ There are many factors affecting the two kinds of flows, including substrate temperature, electric or magnetic field, and so forth.^{7–9} Therefore, it is necessary to explore the mechanisms of fluid flow and the evolution of thin liquid film near the triple line of an evaporating droplet.^{10,11}

For self-rewetting fluids, different mechanisms may exist for droplet evaporation. Self-rewetting fluids refer to dilute aqueous solutions of alcohols with the carbon atom number higher than 4 (such as butanol, pentanol, and hexanol).¹² Compared with

conventional fluids (such as water and methanol), the relationship between the surface tension σ and the temperature T of self-rewetting fluids is nonlinear: for conventional fluids, the surface tension decreases with increasing temperature and $\Delta\sigma/\Delta T < 0$; for self-rewetting fluids, the surface tension decreases with increasing temperature and $\Delta\sigma/\Delta T < 0$ when the temperature is lower than a critical value T_c , whereas it increases with increasing temperature and $\Delta\sigma/\Delta T > 0$ when $T > T_c$. Because of this unique property, evaporation of self-rewetting fluids differs from that of conventional fluids. Normally, when a temperature gradient exists at the liquid–vapor interface, the hot liquid is transported to the cold region mainly by the capillary force for all the fluids as the other forces are negligible. When $T > T_c$, the Marangoni convection is expected to overcome the other forces including the capillary force and to drive the cold liquid to the hot region for self-rewetting fluids.¹³ Droplet evaporation of self-rewetting fluids is a heat- and mass-transfer process with unsteady-state, multi-scale, and multi-physical field coupling. Near the triple line of

Received: January 17, 2018

Revised: February 26, 2018

Published: March 7, 2018

an evaporative droplet of self-wetting fluids, the coupling is more complex because of the inherent physics related to the temporal and spatial evolution of the thin film.

The extended meniscus can be divided into three regions once a drop spreads over a substrate surface: the adsorption layer region, where the liquid is adsorbed on the wall; the thin-film region, where the attractive force of the solid surface is weaker than the long-range molecular forces; and the intrinsic meniscus region, where the capillary forces dominate.¹⁴ The thin-film thickness is usually of nanometer scale. It was shown that the mass flux in this region increases along the interfacial direction toward the contact line.¹⁵ The long-range molecular forces were proved to be crucial for liquid supply into the thin-film region¹⁶ and were found to be dependent on the thin-film profile.^{17–19} This requires theoretical prediction and numerical simulation for the thin-film region. However, direct observation of this region through traditional methods is difficult because of the inherent optical limit. Atomic force microscopy in a tapping mode was successfully used for the characterization of the thin-film profile at about 1 nm away from the contact line,^{20,21} but it is insufficient to further understand how the thin-film profile varies with time. In fact, the thin-film evolution is critical for understanding the thin-film dynamics.^{22–25}

High-precision optical instruments were extensively used to study the internal flow of droplets and the evolution of precursor film that precedes the macroscopic contact line while only a completely wetting fluid can be measured.^{26,27} Instantaneous and nonintrusive approach of nanoparticle image velocimetry with evanescent wave illumination is beneficial for the high-resolution measurement of flow patterns in the thin-film region.²⁸ This technique was derived based on the nanoparticle image velocimetry with multilayers (MnPIV), in which the images were divided into several sublayers by classifying each tracer image into different layers using the fluorescent nanoparticle intensity that correlates with the distance from the wall.²⁹ In our recent work, the local thin-film thickness was approximated by searching the maximum distance between the nanoparticles and the wall using the defined sublayers.²⁸ It was found that the thin-film thickness decreases just before the droplet shrinks. However, high-resolution measurement of the thin-film thickness variation near the triple line during droplet evaporation requires characterization of its temporal and spatial evolution. In this work, this is obtained by using a novel subregion method, which divides the field of view into multiple subregions along the direction of the capillary flow. The spatiotemporal evolution of the local thin-film thickness in droplets containing different kinds of alcohols is compared. In-plane average velocities are also compared to understand their relationships to the thin-film evolution near the triple line.

2. EXPERIMENT

2.1. Experimental Method. The experiment is based on the characteristics of the evanescent wave. Total internal reflection (TIR) occurs at a planar interface between two materials with refractive indices n_1 and n_2 (where $n_1 > n_2$) when the incident angle of the light is greater than the critical incident angle, and an evanescent wave is generated in the lower refractive index or less optically dense medium,²⁹ the intensity of which decays exponentially with the distance normal to the wall. This characteristic is used in multilayer nanoparticle image velocimetry, in which the images are divided into several sublayers based on the nanoparticle intensity

correlating to the distance from the wall.²⁹ This method was validated for its accuracy by many prior research studies^{30–36} and can be extended to explore the evolution of the liquid–vapor interface during thin-film evaporation.

The experimental setup used in this investigation is schematically shown in Figure 1, of which the main body is

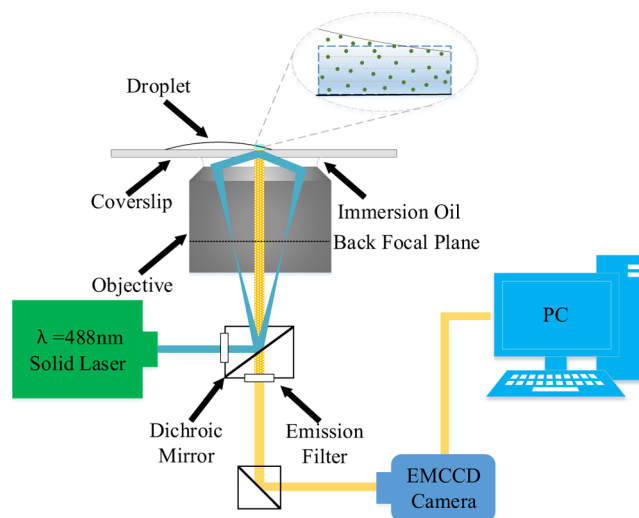


Figure 1. Schematic of experimental setup for interface visualization near the triple line.

an inverted, evanescent wave-based TIR fluorescence (TIRF) microscope (Olympus IX71). The local thin-film thickness variation can be approximated by searching the maximum distance between the nanoparticles and the coverslip, using the defined sublayers which are based on the evanescent wave decaying characteristic. This is briefly introduced as follows. During evaporation, the droplet height decreases gradually until less sublayers are illuminated, and thus, the thin-film thickness at the illumination field may decrease with time. Note that the nanoparticle center in each sublayer is available only if the tracking algorithm is valid; the sublayers with valid velocities are thus used for approximately determining the thin-film thickness. Consequently, the velocity profile near the triple line and the thin-film thickness variation are obtained.

This approach is extended by dividing the field of view into multiple subregions along the direction of the capillary flow, as schematically shown in Figure 2. In each subregion, the extended particle image velocimetry technique can be used to identify the position of the highest nanoparticle, which approximately stands for the local thin-film thickness of the interface. The local thin-film thicknesses are used for data fitting to achieve the thin-film profile. The temporal variation of the thin-film profile is then obtained by repeating the data fitting at different time steps. Accordingly, the temporal and spatial evolution of the thin film near the triple line during droplet evaporation is visualized. The time interval of exposition time for each measurement is chosen as 10 ms, corresponding to the maximum velocity error of about 7%. The accuracy of this method is influenced by many factors including the nonuniform distribution of particles. It was suggested that the accuracy can be improved such that an error less than 4% can be obtained by using the particle-tracking algorithm, carefully choosing the time interval, measuring the window size, and averaging multiple results.^{34,37}

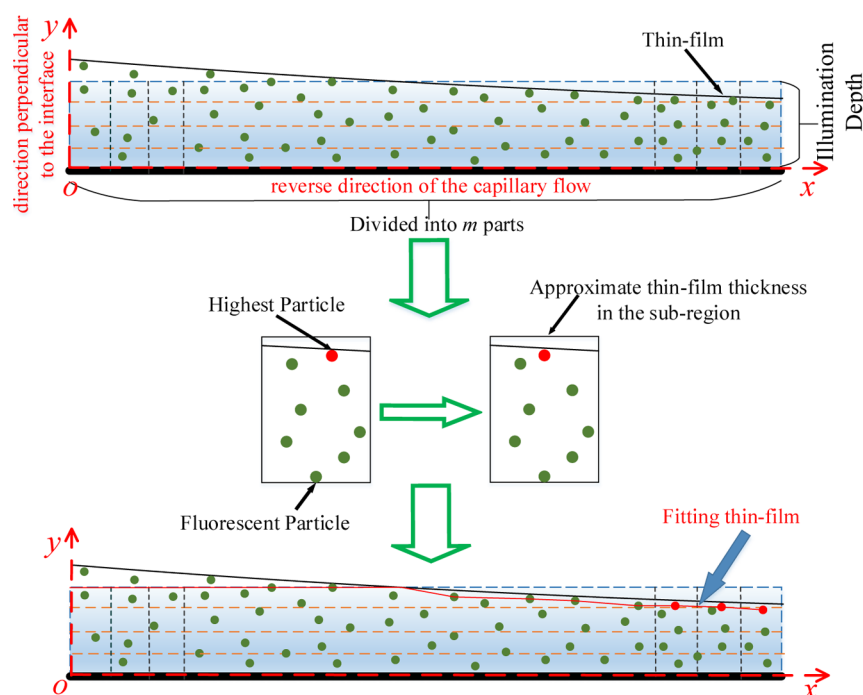


Figure 2. Subregion method for detecting the evolution of the thin film near the triple line.

2.2. Experimental Procedure. The coverslip (Fisherbrand FIS12–545F) is treated before the experiment to guarantee the repeatability of the experimental results. First, it is washed repeatedly using deionized water and immersed in a piranha solution (98% H_2SO_4 and 30% H_2O_2 , with a volume ratio of 3:1) heated by a thermostatic water bath at a temperature of 80 °C for 1 h. Then it is washed again using deionized water and stored in a beaker filled with deionized water. Before each test, the coverslip is immersed in deionized water to sonicate for 10 min; thus, the coverslip is processed to be more hydrophilic because of the hydroxylation of the surface.

Different alcohols (methanol, ethanol, 1-propanol, 1-butanol, 1-pentanol, 1-hexanol, and 1-heptanol) of the same mass are added to deionized water to compare the evaporation of conventional fluids and self-wetting fluids. As the solubility of the alcohols with a high number of carbon atoms decreases with the increasing ratio of the alkyl groups, the solubility of 1-heptanol is minimal (0.12 g/100 mL H_2O at 20 °C). The concentration of the solute is set as 0.10 g/100 mL H_2O , which can ensure that all heptanol is dissolved in water because the environmental temperature is maintained at about 18 °C and the humidity is 37% during the experiment. The samples from deionized water to 1-heptanol solution are labeled as C0–C7, with the numbers being given by their number of carbon atoms (C0–C4 are conventional fluids and C5–C7 are self-wetting fluids). The fluorescent solution with polystyrene tracer nanoparticles is employed in the evanescent-wave-based TIRF velocimetry. The fluorescent nanoparticles (Invitrogen Fluosphere f-8803) are 100 nm in diameter. Using a pipette (Mettler-Toledo Rainin SL-2XLS+), a drop of 2 μL solution seeded with 2 mM, 100 nm nanoparticles is added into 50 mL sample solutions. The concentrations of these solutions are 8.0×10^{-4} w/v %. All the samples are sonicated for 30 min to ensure that the nanoparticles are uniformly distributed.

The evaporation rates of the droplets are measured by using an electronic balance (Mettler-Toledo AB135-S) with a precision of 0.01 mg. The cleansed coverslip is first placed on

the electronic balance, and then 0.5 μL of the testing fluid is taken by using the pipette and dripped onto the coverslip. The droplet mass is measured every 10 s during the entire evaporation process, until it dries out. Experimental results show that the mass of the droplet varies linearly with time; hence, the evaporation rates of the droplets are linearly fitted.

A series of 16-bit images are recorded by an inverted microscope and an electron-multiplying charge-coupled device (EMCCD, Andor Ixon3 Ultra 897) in one measurement with 50 sets of intensity data, which are in-plane-averaged to minimize the random errors. The electronic gain is set as 8. The resolution is set as 256×256 pixels, with an area of 16 μm^2 for each pixel. The exposition time for each measurement is set as 10 ms, and the frame rate for taking the photos is 64 fps.

The static contact angles of the droplets are first measured using a contact angle meter (Powereach JC2000D4M). Then the coverslip is put on the object stage of the microscope. A 60 \times objective (Olympus APON 60 \times) is adjusted to contact with the coverslip bottom through an immersion oil (Olympus Type-F, refractive index: 1.518). A 0.5 μL of the droplet is dripped carefully onto the coverslip to maintain its shape of a spherical cap. The objective is adjusted to focus on the contacted surface of the droplet and the coverslip. The incident angle of the laser beam is adjusted to create TIR at the liquid–solid interface. The evanescent wave generated is used for illuminating the tracer nanoparticles near the solid wall and the triple line. After moving the observation field into the area in the vicinity of triple line, the spreading sessile droplet is pictured every 10 s for the in-plane average velocity measurement.

The refractive index of the borosilicate coverslip is $n_1 = 1.52$, and the refractive index of the water droplets is $n_2 = 1.33$. Therefore, light is totally reflected at the glass–water interface at a critical incident angle of $\phi_c = 61.04^\circ$. Here, the incident angle of excitation light is 68° , and thus, the calculated depth of the illumination field is determined to be about 360 nm. The illuminated region is then divided into four sublayers, with a

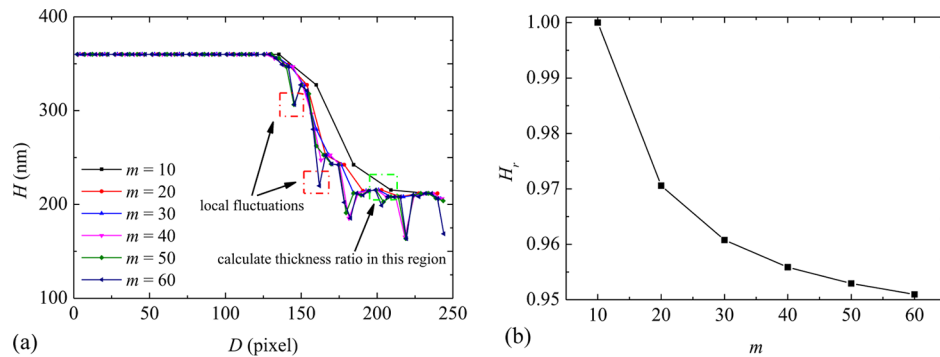


Figure 3. Thin-film thickness variation for the C0 droplet ($t = 90$ s).

thickness of 90 nm for each layer. Fluorescent polystyrene nanoparticles are used as tracers, with each tracer nanoparticle being assigned to one layer based on their distance to the coverslip. Then the thin-film velocity profile near the triple line is obtained by averaging all the particle velocities in each layer. The procedure of experimental preparation for the near-wall velocimetry is the same as that for the in-plane average velocity measurement. A series of 100 images are recorded by EMCCD and are in-plane-averaged to minimize the random errors. These image pairs are then postprocessed using MATLAB toolkits to obtain the near-wall velocity profile.

3. RESULTS AND DISCUSSION

3.1. Interval Numbers. The distances between the particles and the substrate surface can be calculated by using the MnPIV technique. When the thin-film height is less than the illumination depth of the evanescent wave (360 nm), the highest particle on an image is selected to represent the approximate thin-film thickness in the region. The detected area is divided into m segments along the direction of the capillary flow to obtain the trend of the thin-film thickness variation in this region. According to the parameter setting before the experiment, the actual length of the calculated area is 246 pixels and the length of each segment is $246/m$ pixels. The interval numbers should have a significant impact on the accuracy of the fitted thickness for the thin film and thus would be set reasonably.

Taking into account the diffraction limits, the width of each subregion should be higher than the maximum diameter of the particles on the images. For a given optical device, there is a minimum limit for the size of the actual particles on the images. The diameter of particles on the images is calculated by considering the diffraction effect, the geometrical magnification of particles, and the distance between the particles and the focal plane³⁹

$$d_{\text{pi}} = \left[d_{\text{diff}}^2 + 4M^2a^2 + \frac{M^2z_f^2d_a^2}{(s_{\text{ob}} + z_{\text{fp}})^2} \right]^{1/2} \quad (1)$$

where d_{diff} is the diffraction-limited spot size, M is the magnification of lens, a is the radius of the particle, z_{fp} is the distance between the center of the particle and the focal plane, d_a is the aperture diameter, and s_{ob} is the object distance. If the particles are in contact with the wall, then the last item in the upper form can be neglected. Meinhart and Wereley⁴⁰ derived d_{diff} for infinity-corrected optics

$$d_{\text{diff}} = 1.22M\lambda \left[\left(\frac{n_0}{\text{NA}} \right)^2 - 1 \right]^{1/2} \quad (2)$$

where NA is the numerical aperture of the objective lens and λ is the wavelength. For a CCD camera, with a pixel size of 16 μm and a 60 \times magnification lens, the maximal diameter of the particle on the digital image is about 3.6 pixels; thus, the maximum interval number is about 68.

The calculated displacement of the particles is not exactly consistent with its actual value, which means that the calculated positions of the particles are not identical with their actual locations. This difference will lead to some errors in the process of dividing the particles into subregions using the calculated positions, and thus, a subregion may have particles which should have been divided into a proper subregion if the calculated and the actual positions are identical. Therefore, the influence of the time interval Δt between two images on the accuracy of the MnPIV technology is investigated. The results show that the calculation error is related to the distance between the particles and the wall, and the largest errors are in layer I, the thinnest layer, and the one next to the wall, where only about 20% of particle images are “matched” within an image pair over this 30 nm thick layer.⁴¹ In this experiment, the time interval is set as 10 ms, and according to the above-mentioned method, the maximum error of the velocity calculation is about 10%. At the later stage of measurement, the maximum displacement of particles is about 4 pixels. The influence of interval numbers on fitting the thin-film thickness is defined by $\Delta\epsilon/L$, where $\Delta\epsilon$ is the deviation of particle displacement and L is the width of the subregion. The result shows that the possibility of thin-film fluctuation increases with increasing interval numbers. Brownian motion should be considered when setting the interval numbers. The longitudinal motion of particles is more susceptible to the Brownian motion relative to the transverse motion of the particles. Particles may therefore appear in only one of the two frames of an image pair, resulting in the so-called mismatched particle images, which effectively increase the noise and uncertainty of velocities obtained by this technique. It is found that the mismatched particles as a fraction of the total number of particles within an image pair, F , increase rapidly with Δt with a relationship $F \propto \Delta t^{0.4}$.⁴¹ According to the parameter setting in the experiment, F is calculated to be about 53%. The influence of mismatched particles on the fitting thin films increases with increasing interval numbers, and the thin films exhibit partial fluctuations when the set interval number is too large.

Note that the highest particle is not completely at the center of the subregion because of the random distribution of particles

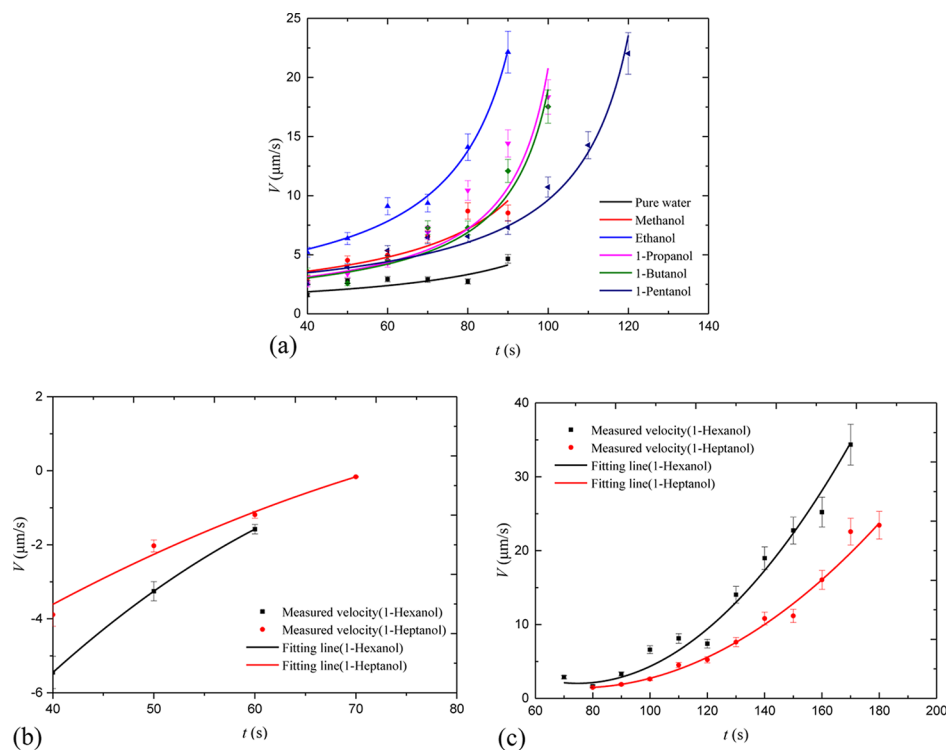


Figure 4. In-plane average velocities in the detection areas near the triple lines.

and the influence of Brownian motion. For example, the liquid film thicknesses (H) of C0 (at 90 s) are calculated with interval numbers (m) varying from 10 to 60, as shown in Figure 3a. When comparing the variations of liquid film thicknesses, apparent local fluctuations appear at the interval numbers of 40–60 as shown in the left (red) dashed line squares in Figure 3a, meaning that high interval numbers are not conducive to high-precision prediction. Local fluctuations may occur at the regions where insufficient tracer particles are grouped to perform efficient tracking of particle positions. For the interval numbers of 10–30, no obvious local fluctuations are observed. To obtain the thin-film profile with as much details as possible, the interval number of 30 is thus chosen for the calculation of thickness.

To further examine the reasonability of choosing a compromised interval number, the ratio of the film thickness is defined to show the trend when using different interval numbers. First, a region in which less fluctuations occur for all the interval numbers is selected representatively, as shown in the right (green) dashed line square in Figure 3a, to diminish the influence of insufficient tracer particles. Then, the film thickness determined by the interval number $m = 10$ is chosen as the reference value, and the ratio of the film thicknesses determined by other interval numbers to the reference value is termed as the thickness ratio, H_r . The calculation shown in Figure 3b clearly shows that with an increase in the interval numbers, the thickness ratio decreases gradually, but it varies slightly with m varying from 30 to 60. It also indicates that when m is rather small, the actual position of the highest particle differs greatly from the center of the subregion. Therefore, the interval number is chosen with compromise as 30, taking into account the error of velocity calculation and the effect of Brownian motion.

Precaution is also taken to improve the accuracy of fitting the liquid film. The inhomogeneity of the incident light and the

actual size distribution of the particles result in the difference between the reference gray scale and the actual gray scale of the 100 nm particles on the wall surface, and the maximum difference of the gray scale Δg is about 100. According to the characteristic of the evanescent wave, the distance between the particles and the surface of the wall can be expressed as

$$h = z \ln \frac{g_0}{g} \quad (3)$$

where z is the intensity-based e^{-1} penetration depth of the evanescent wave or the distance into the less-dense medium from the interface where the wave intensity is reduced by a factor of $1/e$, g is the gray scale of the fluorescent particles, and g_0 is the gray scale of the particles at the wall surface ($y = 0$). The error of height of the particles is expressed as

$$\Delta h = z_p \ln \frac{g_0 + \Delta g}{g_0} \quad (4)$$

In the experiment, the incident angle of the excitation light is 68° and z_p is about 90 nm. The reference gray scale of the 100 nm particles on the wall surface in the experiment is 811.57. The maximum difference Δh between the calculated value and the actual value of h for the 100 nm particles is about 10 nm, which can affect the accuracy of the fitted thin liquid film.

3.2. Velocity Fields. The initial contact angles θ_0 before the evaporation of C0–C7 droplets, which have the same volume of $0.5 \mu\text{L}$, are measured to be 7.22° , 6.25° , 5.81° , 6.23° , 7.25° , 7.67° , 8.94° , and 9.03° , respectively. It shows that the wettability of self-rewetting fluids is weaker than that of conventional fluids. The wettability of self-rewetting fluids also reduces gradually with an increasing number of carbon atoms. This is due to the gradual increase of the proportion of the alkyl groups in the self-rewetting fluids under the same mass of the solute. The evaporation rates for C0–C7 droplets are

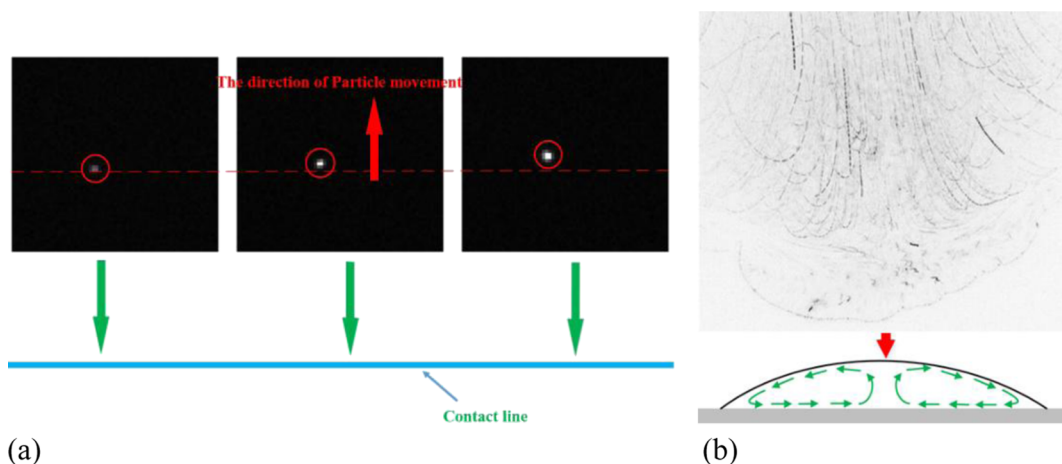


Figure 5. Motion of fluorescent nanoparticles in 1-hexanol solution (C6 droplet).

determined as 0.00471, 0.00526, 0.00578, 0.00520, 0.00488, 0.00398, 0.00387, and 0.00383 mg/s, respectively. It shows that the evaporation rates of C1 and C2 droplets are slightly higher than that of the C0 droplet, and the evaporation rates of C5–C7 droplets are remarkably smaller than that of the C0 droplet. This indicates that the evaporation rates of the droplets are affected by the types of solutes. Compared with the conventional fluid droplets, the evaporation rate of self-wetting fluid droplets is smaller, which can be attributed to the factors including the different mass flux at the liquid–vapor interface because of the various internal flow mechanisms.

The in-plane average velocities in the field of view are first measured during droplet evaporation to understand the effect of fluid properties on evaporation. Using the evanescent wave illumination, the particle image velocimetry technique is extended to the measurement of the average velocities of 40 s after the droplets are dripped onto the coverslip. The fluorescent intensity images for the average velocity measurement are obtained at the position where the field of view is about 40 μm next to the contact line observed in this experiment.

As shown in Figure 4a, the measured average velocity V fits well with an increasing function $V \approx (t_f - t)^{-1}$ for the samples of C0–C5, where t_f is the starting time of the contact line depinning and t is the evaporation time. This is also consistent with the analysis of ring stains after droplet evaporation;³⁸ therefore, the capillary flow should be the main contributor to the fluid flow near the triple line. However, the above fitting function is not applicable for self-wetting fluid (C6 and C7) droplets.

For instance, for the C6 droplet, the particles move toward the droplet center, which is opposite to the capillary flow, in the illuminated range of the evanescent wave during the initial stage of evaporation, as shown in Figure 5a. The internal flow of droplets is then recorded using a 4 \times objective for further investigation of the evaporation of self-wetting fluid droplets. The time interval between two images is set as 10 ms, and the trajectory of the particles is obtained by the synthesis of one image from the 20 images.

At the initial stage of evaporation, there is a vortex directing from the top region of the droplet of self-wetting fluids to the three-phase contact line, then it turns to the inside of the droplet, as shown in Figure 5b. The vortex is produced by the Marangoni convection caused by the concentration gradient

because of the saturated vapor pressure of the high carbon alcohol and the surface tension gradient at the liquid–vapor interface. During evaporation, the intensity of the vortex decreases gradually.

When the evaporation time t is larger than the disappearance time of the vortex, t_v , the capillary flow is dominant. It is found that the quadratic function is more suitable for the in-plane average velocities of the self-wetting fluid droplets. As shown in Figure 4b,c, the evaporation of C6 and C7 droplets can be divided into two stages. In the first stage, the expressions of the velocities for C6 and C7 can be fitted as

$$V = a_1 + b_1(t - t_v) + c_1(t - t_v)^2 \quad (5)$$

where $a_1 = -0.3 \mu\text{m/s}$, $b_1 = 0.11 \mu\text{m}/(\text{s}\cdot^\circ\text{C})$, $c_1 = -0.0023 \mu\text{m}/(\text{s}\cdot^\circ\text{C}^2)$, and t_v is about 70 s for C6 and 65 s for C7. In the second stage, the expressions of velocities are fitted as

$$V = a_2 + b_2(t - (t_f - t_v)) + c_2(t - (t_f - t_v))^2 \quad (6)$$

where $a_2 = 5 \mu\text{m/s}$, $b_2 = 0.18 \mu\text{m}/(\text{s}\cdot^\circ\text{C})$, $c_2 = 0.0025 \mu\text{m}/(\text{s}\cdot^\circ\text{C}^2)$, and t_f is about 170 s for C6 and 250 s for C7. Therefore, the relationship between the in-plane average velocities and the evaporation time for conventional fluids (C0–C3) is $V \approx (t_f - t)^{-1}$; for self-wetting fluids with a low number of carbon atoms (C4 and C5), the relationship is still $V \approx (t_f - t)^{-1}$; for those with a higher number of carbon atoms (C6 and C7), the relationship is $V \approx (t - t_v)^2$ at the earlier stage of evaporation and $V \approx (t - (t_f - t_v))^2$ at the later stage. Note that both $V \approx (t_f - t)^{-1}$ and eq 6 can be applied to the self-wetting fluids of C4 and C5 because t_v is very short (<30 s) and t_f is about 100 s for C4 and 120 s for C5, which are apparently shorter than those of the self-wetting fluids of C6 and C7. Therefore, the proposed novel correlation could be widely used for the self-wetting fluids studied in this work and even for those with a higher number of carbon atoms.

3.3. Variation of Thin-Film Thickness. Using the recorded 16-bit images with 256×256 pixels, an effective calculation region of field of view of 246×246 pixels is available to detect the evolution of thin-film thickness. The magnification of the imaging system is 60, which corresponds to $0.267 \mu\text{m}/\text{pixel}$; thus, a field of view of $65.42 \times 65.42 \mu\text{m}^2$ is obtained. Here, 30 subregions, with a width of about $2.18 \mu\text{m}$ for each subregion, are used for the calculations. We denote o as the origin which lies on the farthest side of the field of view to the contact line, D as the distance from the origin in the field

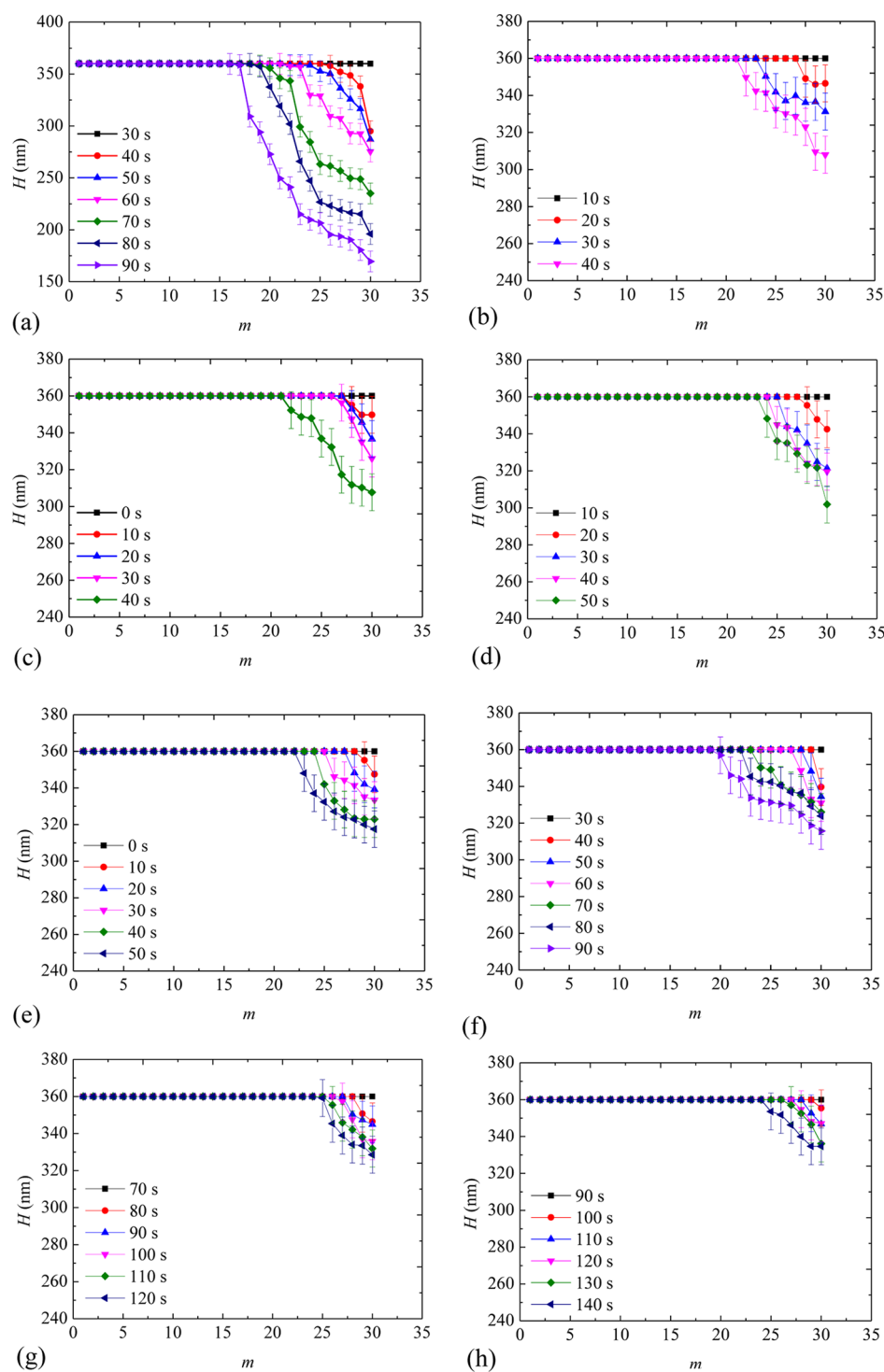


Figure 6. Evolution of thin-film thickness in the detection areas for different droplets.

of view, and H as the local thin-film thickness. Figure 6 shows that the evolution of local thin-film thickness for the droplets is different.

At an initial stage of the experiment, the evaporation mode of the droplets for all samples is CCR mode, that is, the contact radius is constant and the contact angle decreases gradually. Along with the evaporation, the contact angle decreases gradually and the liquid film becomes thinner. Because the thin-film thickness on the side of the detection region near the contact line is relatively small as compared to the other side, its

interface pioneers to be illuminated by the evanescent wave. The thin-film thickness in the subregion nearest to the contact line is selected to compare the evaporation modes of different samples. To reduce the error caused by random motion of particles, the largest particle of two adjacent subregions is selected to represent the liquid film thickness of this area, as shown in Figure 7. As the droplet evaporates, its contact angle decreases gradually; when it evolves into the microscopic critical contact angle, θ_c , the contact line begins to move and the evaporation mode changes to the CCA mode, namely, the

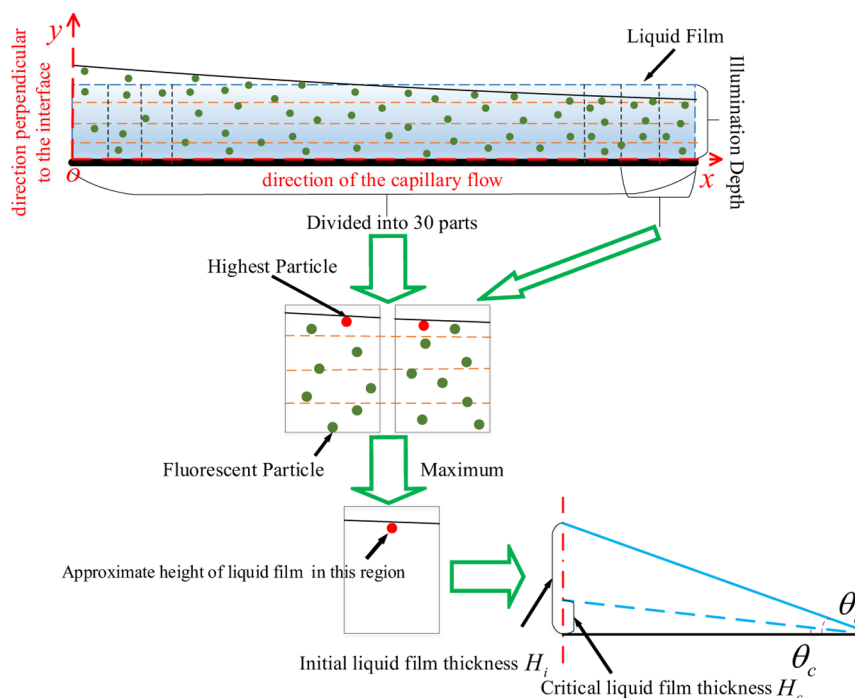


Figure 7. Schematic for determining the microscopic critical contact angle.

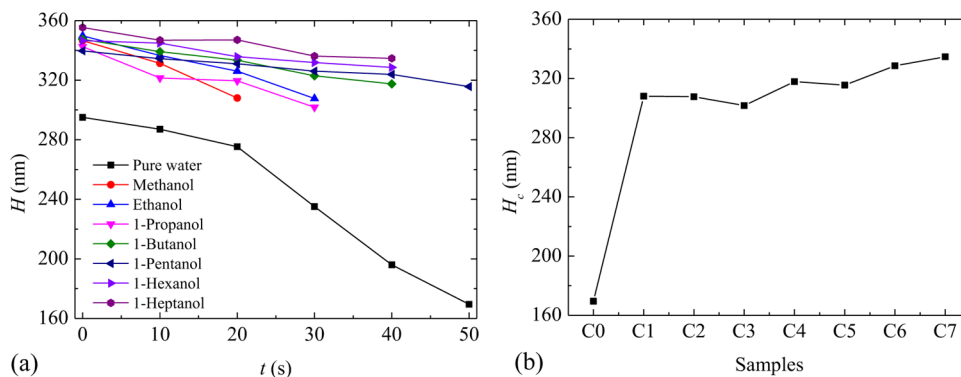


Figure 8. Evolution of thin-film thickness in the subregions nearest to the triple line for C0–C7 droplets.

contact angle is constant and the contact radius decreases gradually. Thus, there is a critical thin-film thickness, H_c at which the evaporation mode changes.

The thin-film thickness variation with the evaporation time is shown in Figure 8a, from which the critical thin-film thickness can be derived. As shown in Figure 8b, the addition of alcohols seems to be beneficial for improving the critical thin-film thickness as compared with that of water. The microscopic critical contact angles of the droplets are calculated to be 0.2305° , 0.4202° , 0.4198° , 0.4116° , 0.4335° , 0.4304° , 0.4481° , and 0.4566° for C0–C7 samples. Compared with the conventional fluids (C0–C3 samples), the microscopic critical contact angles of the self-rewetting fluid droplets are larger and generally increase with an increasing number of carbon atoms. This is determined by the proportion of hydrogen bonds in the alcohol molecules and the surface tension characteristics of the fluids.

The depinning of the contact lines is influenced by the energy barrier that prevents the triple line movement. Using Young's equation at the equilibrium state, $\sigma_{sl} - \sigma_{sg} = \sigma_{lg} \cos \theta_0$,

the corresponding Gibbs free energy denoted by $G = \sigma_{lg}A + \pi R^2(\sigma_{sl} - \sigma_{sg})$ can be rewritten as⁴²

$$G = \sigma_{lg}\pi R^2 \left(\frac{2}{1 + \cos \theta} - \cos \theta_0 \right) \quad (7)$$

where R is the contact radius of the droplet, θ is the actual contact angle of the droplet, θ_0 is the equilibrium contact angle established at the atomically flat surface, A is the liquid–vapor interfacial area of the spherical cap, and σ_{lg} , σ_{sl} , and σ_{sg} are the surface tensions at the liquid–gas, solid–liquid, and solid–gas interfaces, respectively. When the droplet is out of equilibrium with contact radius $R = R_0 + \delta R$, the excess free energy $\delta G = G(R) - G(R_0)$. The excess free energy per unit length of the triple line due to the deviation of state from the equilibrium one for the same droplet volume can be derived in terms of change of contact angle or radius as⁴³

$$\delta \tilde{G} = \frac{\delta G}{2\pi R} = \frac{(\delta \theta)^2}{4\pi R} \left(\frac{d^2 G}{d\theta^2} \right)_{\theta=\theta_0} = \frac{\sigma_{lg} R (\delta \theta)^2}{2(2 + \cos \theta_0)} \quad (8)$$

When the contact line depins, $\delta\tilde{G}$ is simply equivalent to the energy barrier U .⁴² In the experiment, the surface tension σ_{lg} values of the samples of C0–C7 are 70.59, 70.33, 69.99, 67.75, 66.09, 65.54, 52.12, and 38.18 mN/m. The contact radius R can be calculated by the initial contact angle θ_0 and the volume of droplet, and $\delta\theta$ can be obtained by the difference between the initial contact angle θ_0 and the critical contact angle θ_c . Therefore, the energy barrier U can be calculated by eq 8.

The ratios of energy barriers for different samples (C1–C7) to the reference energy barrier for the water sample (C0), U/U_0 , are named as reduced energy barriers. The result shown in Figure 9 indicates that the self-rewetting fluids are beneficial for

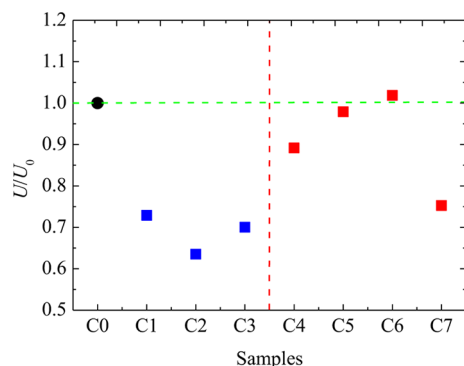


Figure 9. Reduced energy barriers of the contact lines for C0–C7 droplets.

reducing the energy barriers of the contact lines, and the contribution of self-rewetting fluids to the reduction of energy barriers is less than that of conventional alcoholic solutions, such as methanol solution, ethanol solution, and so forth.

It can be seen from Figure 8a that basically the thin-film thickness H changes linearly with the evaporation time t in the subregions, and thus, the rates of thin-film thickness variation, $\Delta H/\Delta t$, can be obtained by linear fitting. Figure 10 shows that

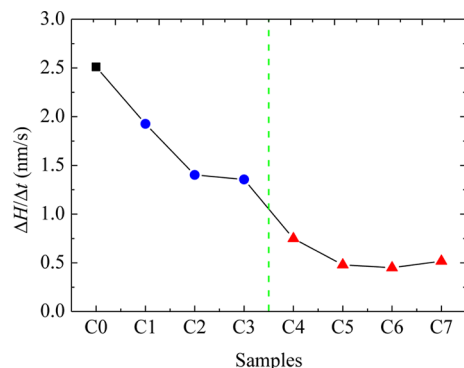


Figure 10. Rates of thin-film thickness variation with respect to time in C0–C7 droplets.

the rates for C0–C7 droplets are 2.51, 1.93, 1.40, 1.36, 0.75, 0.48, 0.45, and 0.52 nm/s, respectively. The general trend clearly indicates that the thin-film thickness of water changes faster than those of the other aqueous alcohol solutions. Also, the rates of thin-film thickness variation of the self-rewetting fluids are apparently smaller than that of the conventional fluids, which indicates that the introduction of alcohols with a high number of carbon atoms to water can substantially suppress the evaporation of droplets. This is attributed to the

presence of the Marangoni convection in the self-rewetting fluid droplets from the region near the contact line to the droplet top, which transports the fluids to the droplet center and hence weakens the contribution of thin-film evaporation to the entire heat and mass transfer at the liquid–vapor interface. In addition, the inhibition of self-rewetting fluids on the evaporation is more obvious as the number of carbon atoms (i.e., the proportion of alkyl groups in molecules) increases. This is due to the fact that the gradient of surface tension increases with the increase in the proportion of alkyl groups, and thus, the intensity of the Marangoni convection increases accordingly, which has a notable impact on the evaporation of droplets.

4. CONCLUSIONS

Evaporation of droplets of conventional fluids and self-rewetting fluids near the triple line was observed to capture insights on how the self-rewetting fluids influence the evaporation mode. The evaporation rates of the droplets were first obtained. It shows that the addition of alcohols (methanol and ethanol) with low carbon number can increase the evaporation rate, whereas the introduction of alcohols with high carbon number can substantially reduce the evaporation rate. The in-plane average velocities in the field of view were then measured during droplet evaporation, and the self-rewetting fluids form a vortex because of the Marangoni convection at the beginning of evaporation which differs from that of conventional fluids. The relationship between the average velocities and evaporation time for conventional fluids is $V \approx (t_f - t)^{-1}$. For self-rewetting fluid droplets, the relationship changes from $V \approx (t - t_r)^2$ to $V \approx (t - (t_f - t_r))^2$ because of the presence of the vortex. Using the proposed subregion method, the temporal and spatial evolution of the thin film near the triple line during droplet evaporation was obtained. Self-rewetting fluids are conducive to enlarge the microscopic critical contact angle and slow down the rate of thin-film thickness variation. The inhibition on evaporation is more obvious as the number of carbon atoms increases. This work also reveals that the capability of reducing the energy barrier for the self-rewetting fluids is weaker than that for the conventional fluids.

AUTHOR INFORMATION

Corresponding Author

*E-mail: lpzhou@ncepu.edu.cn. Phone: +86 10 6177 1439 (L.P.).

ORCID

Leping Zhou: 0000-0001-9582-4237

Notes

The authors declare no competing financial interest.

ACKNOWLEDGMENTS

The authors are grateful to the financial support from the National Natural Science Foundation of China (no. 91634115).

NOMENCLATURE

a	radius (m)
aperture	
A	interfacial area (m^2)
a_1, a_2	constants ($\mu\text{m}/\text{s}$)
b_1, b_2	constants ($\mu\text{m}/(\text{s} \cdot ^\circ\text{C})$)
c_1, c_2	constants ($\mu\text{m}/(\text{s} \cdot ^\circ\text{C}^2)$)

d	diameter (m)
D	distance (m)
F	fraction (%)
g	gray scale (-)
G	Gibbs free energy (J)
h	particle–wall distance (m)
H	local thin-film thickness (m)
H_r	thickness ratio
L	width of the subregion (m)
m	interval number
M	magnification of lens
n	refractive index
NA	numerical aperture
R	contact radius (m)
s	distance (m)
t	time (s)
T	temperature ($^{\circ}\text{C}$)
U	energy barrier (J)
V	thinning velocity (m/s)
z	distance (m)

■ GREEK SYMBOLS

ε	displacement of particles (m)
ϕ	incident angle ($^{\circ}$)
λ	wavelength (m)
θ	contact angle ($^{\circ}$)
σ	surface tension (N/m)

■ SUBSCRIPTS

0	initial, reference, or equilibrium
a	radius (m)
aperture	
c	critical
diff	diffraction-limited
f	drying
fp	focal plane
lg	liquid–gas interface
o	origin
ob	object
pi	particles on image
sg	solid–gas interface
sl	solid–liquid interface
v	vortex

■ REFERENCES

- (1) Calvert, P. Inkjet printing for materials and devices. *Chem. Mater.* **2001**, *13*, 3299–3305.
- (2) Kimura, M.; Misner, M. J.; Xu, T.; Kim, S. H.; Russell, T. P. Long-range ordering of diblock copolymers induced by droplet pinning. *Langmuir* **2003**, *19*, 9910–9913.
- (3) Wu, J.; Wang, R.; Yu, H.; Li, G.; Xu, K.; Tien, N. C.; Roberts, R. C.; Li, D. Inkjet-printed microelectrodes on PDMS as biosensors for functionalized microfluidic systems. *Lab Chip* **2015**, *15*, 690–695.
- (4) Picknett, R. G.; Bexon, R. The evaporation of sessile or pendant drops in still air. *J. Colloid Interface Sci.* **1977**, *61*, 336–350.
- (5) Shanahan, M. E. R. Simple theory of “stick-slip” wetting hysteresis. *Langmuir* **1995**, *11*, 1041–1043.
- (6) Sempels, W.; De Dier, R.; Mizuno, H.; Hofkens, J.; Vermant, J. Auto-production of biosurfactants reverses the coffee ring effect in a bacterial system. *Nat. Commun.* **2013**, *4*, 1757.
- (7) Parsa, M.; Harmand, S.; Sefiane, K.; Bigerelle, M.; Deltombe, R. Effect of substrate temperature on pattern formation of nanoparticles from volatile drops. *Langmuir* **2015**, *31*, 3354–3367.
- (8) Eral, H. B.; Augustine, D. M.; Duits, M. H. G.; Mugele, F. Suppressing the coffee stain effect: how to control colloidal self-assembly in evaporating drops using electrowetting. *Soft Matter* **2011**, *7*, 4954–4958.
- (9) Xu, W.; Yao, Y.; Klassen, J. S.; Serpe, M. J. Magnetic field assisted programming of particle shapes and patterns. *Soft Matter* **2015**, *11*, 7151–7158.
- (10) Hu, H.; Larson, R. G. Evaporation of a sessile droplet on a substrate. *J. Phys. Chem. B* **2002**, *106*, 1334–1344.
- (11) Savino, R.; di Francescantonio, N.; Fortezza, R.; Abe, Y. Heat pipes with binary mixtures and inverse Marangoni effects for microgravity applications. *Acta Astronaut.* **2007**, *61*, 16–26.
- (12) Savino, R.; Cecere, A.; Di Paola, R. Surface tension-driven flow in wickless heat pipes with self-rewetting fluids. *Int. J. Heat Fluid Flow* **2009**, *30*, 380–388.
- (13) Abe, Y. About self-rewetting fluids, Possibility as a new working fluid. *Therm. Sci. Eng.* **2003**, *12*, 9–18.
- (14) Wang, H.; Garimella, S. V.; Murthy, J. Y. Characteristics of an evaporating thin film in a microchannel. *Int. J. Heat Mass Transfer* **2007**, *50*, 3933–3942.
- (15) Deegan, R. D.; Bakajin, O.; Dupont, T. F.; Huber, G.; Nagel, S. R.; Witten, T. A. Contact line deposits in an evaporating drop. *Phys. Rev. E: Stat. Phys., Plasmas, Fluids, Relat. Interdiscip. Top.* **2000**, *62*, 756.
- (16) Wayner, P. C.; Kao, Y. K.; LaCroix, L. V. The interline heat transfer coefficient of an evaporating wetting film. *Int. J. Heat Mass Transfer* **1976**, *19*, 487–492.
- (17) DasGupta, S.; Schonberg, J. A.; Wayner, P. C. Investigation of an evaporating extended meniscus based on the augmented Young-Laplace equation. *J. Heat Transfer* **1993**, *115*, 201–208.
- (18) Hallinan, K. P.; Kim, S. J.; Chang, W. S. Evaporation from an extended meniscus for nonisothermal interfacial conditions. *J. Thermophys. Heat Transfer* **1994**, *8*, 709–716.
- (19) Park, K.; Noh, K.-J.; Lee, K.-S. Transport phenomena in the thin-film region of a micro-channel. *Int. J. Heat Mass Transfer* **2003**, *46*, 2381–2388.
- (20) Deng, Y.; Chen, L.; Yu, J.; Wang, H. Nanoscopic morphology of equilibrium thin water film near the contact line. *Int. J. Heat Mass Transfer* **2015**, *91*, 1114–1118.
- (21) Mehri, A. A.; Wang, H. Evaporating thin film profile near the contact line of a partially wetting water droplet under environmental heating. *Int. J. Heat Mass Transfer* **2017**, *107*, 1–5.
- (22) Dallaston, M. C.; Tseluiko, D.; Kalliadasis, S. Dynamics of a thin film flowing down a heated wall with finite thermal diffusivity. *Phys. Rev. E: Stat. Phys., Plasmas, Fluids, Relat. Interdiscip. Top.* **2016**, *1*, 073903.
- (23) Witelski, T. P.; Bernoff, A. J. Dynamics of three-dimensional thin film rupture. *Phys. D* **2000**, *147*, 155–176.
- (24) Oron, A.; Davis, S. H.; Bankoff, S. G. Long-scale evolution of thin liquid films. *Rev. Mod. Phys.* **1997**, *69*, 931.
- (25) Thiele, U. Note on thin film equations for solutions and suspensions. *Eur. Phys. J.: Spec. Top.* **2011**, *197*, 213–220.
- (26) Hoang, A.; Berteloot, G.; Sharif-Kashani, P.; Kavehpour, H. P. Dynamic measurement of microfilms and nanofilms of fluids using fluorescence microscopy. *Exp. Fluids* **2012**, *52*, 1657–1662.
- (27) Houssainy, S.; Kavehpour, H. P. Free-surface profile of evaporative liquids at the vicinity of the contact line. *J. Coat. Technol. Res.* **2015**, *12*, 863–867.
- (28) Xiao, C.; Zhou, L.; Sun, Z.; Du, X.; Yang, Y. Near-wall fluid flow near the pinned contact line during droplet evaporation. *Exp. Therm. Fluid Sci.* **2016**, *72*, 210–217.
- (29) Axelrod, D.; Burghardt, T. P.; Thompson, N. L. Total internal reflection fluorescence. *Annu. Rev. Biophys. Bioeng.* **1984**, *13*, 247–268.
- (30) Zettner, C.; Yoda, M. Particle velocity field measurements in a near-wall flow using evanescent wave illumination. *Exp. Fluids* **2003**, *34*, 115–121.
- (31) Li, H. F.; Sadr, R.; Yoda, M. Multilayer nano-particle image velocimetry. *Exp. Fluids* **2006**, *41*, 185–194.

- (32) Sadr, R.; Yoda, M.; Zheng, Z.; Conlisk, A. T. An experimental study of electro-osmotic flow in rectangular microchannels. *J. Fluid Mech.* **2004**, *506*, 357–367.
- (33) Sadr, R.; Hohenegger, C.; Li, H.; Mucha, P. J.; Yoda, M. Diffusion-induced bias in near-wall velocimetry. *J. Fluid Mech.* **2007**, *577*, 443–456.
- (34) Li, H. F.; Yoda, M. Multilayer nano-particle image velocimetry (MnPIV) in microscale Poiseuille flows. *Meas. Sci. Technol.* **2008**, *19*, 075402.
- (35) Lasne, D.; Maali, A.; Amarouchene, Y.; Cognet, L.; Lounis, B.; Kellay, H. Velocity profiles of water flowing past solid glass surfaces using fluorescent nanoparticles and molecules as velocity probes. *Phys. Rev. Lett.* **2008**, *100*, 214502.
- (36) Franken, M. J. Z.; Poelma, C.; Westerweel, J. Nanoscale contact line visualization based on total internal reflection fluorescence microscopy. *Opt. Express* **2013**, *21*, 26093–26102.
- (37) Sadr, R.; Li, H.; Yoda, M. Impact of hindered Brownian diffusion on the accuracy of particle-image velocimetry using evanescent-wave illumination. *Exp. Fluids* **2005**, *38*, 90–98.
- (38) Deegan, R. D.; Bakajin, O.; Dupont, T. F.; Huber, G. Capillary flow as the cause of ring stains from dried liquid drops. *Nature* **1997**, *389*, 827–829.
- (39) Olsen, M. G.; Adrian, R. J. Out-of-focus effects on particle image visibility and correlation in microscopic particle image velocimetry. *Exp. Fluids* **2000**, *29*, S166–S174.
- (40) Meinhart, C. D.; Wereley, S. T. The theory of diffraction-limited resolution in microparticle image velocimetry. *Meas. Sci. Technol.* **2003**, *14*, 1047–1053.
- (41) Li, H.; Sadr, R.; Yoda, M. Multilayer nano-particle image velocimetry. *Exp. Fluids* **2006**, *41*, 185–194.
- (42) Sun, Z.; Zhou, L.; Xiao, C.; Du, X.; Yang, Y. Nanoparticle motion and deposition near the triple line in evaporating sessile water droplet on a superhydrophilic substrate. *Exp. Therm. Fluid Sci.* **2016**, *76*, 67–74.
- (43) Shanahan, M. E. R. Simple theory of “stick-slip” wetting hysteresis. *Langmuir* **1995**, *11*, 1041–1043.